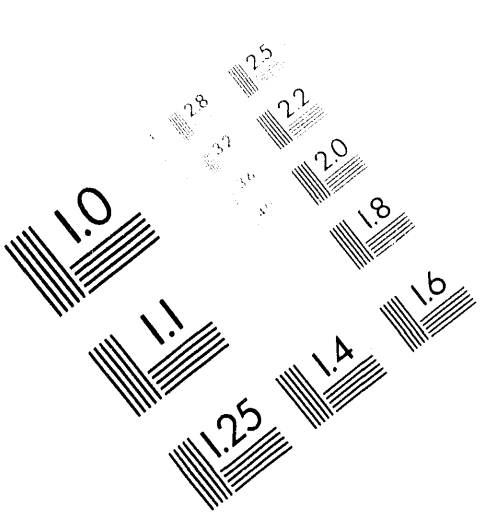

AIIM

Association for Information and Image Management
1100 Wayne Avenue, Suite 1100
Silver Spring, Maryland 20910
301/587-8202

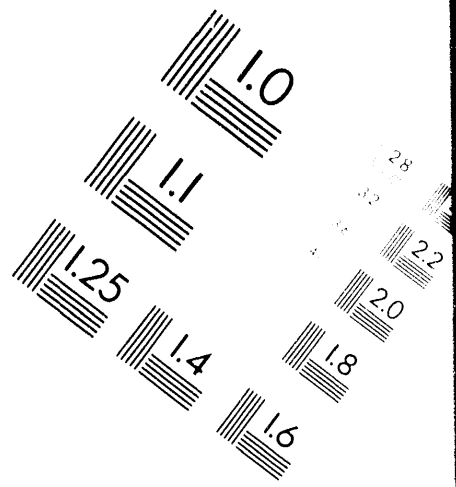

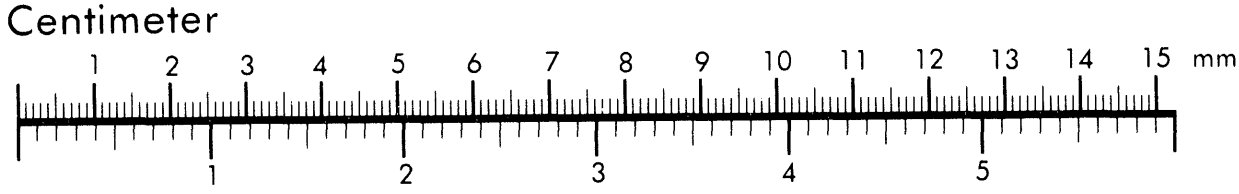

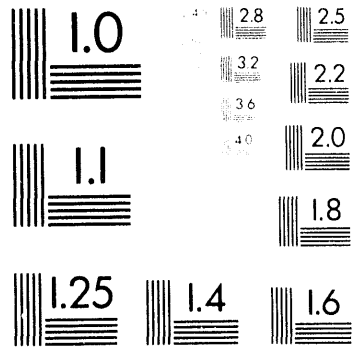

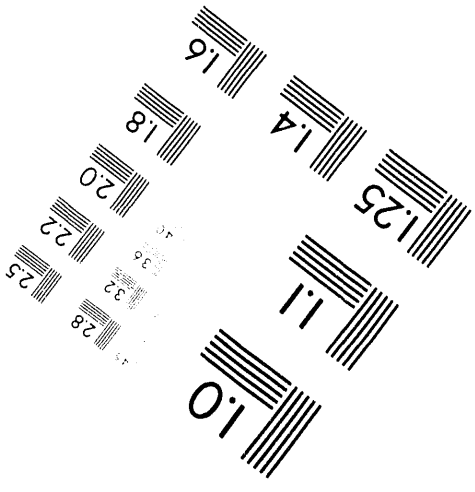

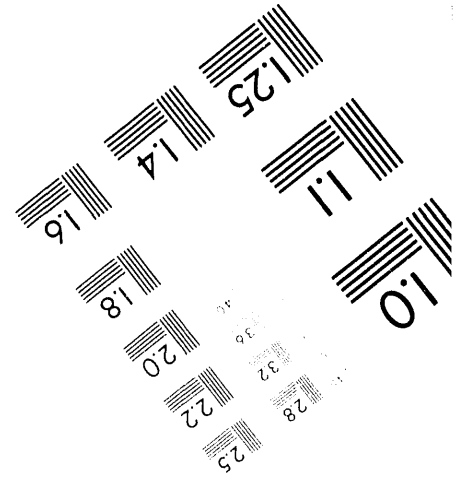

MANUFACTURED TO AIIM STANDARDS
BY APPLIED IMAGE, INC.

1 of 1

LA-12732-SR
Status Report

UC-906
Issued: July 1994

Status and Test Report on the LANL-Boeing APLE/HPO Flying-Wire Beam-Profile Monitor

M. Wilke
D. Barlow
C. Fortgang
J. Gilpatrick
*R. Greegor**
R. Meyer
A. Rendon
D. Warren

**The Boeing Company, P.O. Box 3999, Seattle, WA 98124*

Los Alamos
NATIONAL LABORATORY
Los Alamos, New Mexico 87545

Status and Test Report on the LANL-Boeing APLE/HPO Flying-Wire Beam-Profile Monitor

by

M. Wilke, D. Barlow, C. Fortgang, J. Gilpatrick, R. Greegor, R. Meyer, A. Rendon and D. Warren

ABSTRACT

The High-Power Oscillator (HPO) demonstration of the Average Power Laser Experiment (APLE) is a collaboration by Los Alamos National Laboratory and Boeing to demonstrate a 10 kW average power, 10 μm free electron laser (FEL). As part of the collaboration, Los Alamos National Laboratory (LANL) is responsible for many of the electron beam diagnostics in the linac, transport, and laser sections. Because of the high duty factor and power of the electron beam, special diagnostics are required. This report describes the flying wire diagnostic required to monitor the beam profile during high-power, high-duty operation. We describe the diagnostic and prototype tests on the Los Alamos APLE Prototype Experiment (APEX) FEL. We also describe the current status of the flying wires being built for APLE.

I. INTRODUCTION

Figure 1[1] is a schematic of the average power laser experiment/high-power oscillator demonstration (APLE/HPO) linac and free electron laser (FEL). Figure 2[1] shows the pulse structure of the APLE/HPO RF, linac electron beam and the FEL output. The machine parameters are summarized in Table I. During the startup phase, the beam shape and size can be monitored with standard imaging techniques using phosphors, quartz Cherenkov screens or optical transition radiation (OTR) screens for 9 or 27 MHz micropulse repetition rates with macropulse lengths of up to 10 s of microseconds in length and micropulse charges of a few nanocoulombs.

When HPO is switched to the high-duty-factor mode of operation, which may reach 25% duty, the screens are no longer useful because the intense electron beams would destroy them within 1 macropulse. During the macropulse, the average beam current for 27 MHz operation with 8.5 nC per micropulse is I_{avg} = 0.23 amps. Beam position monitors are a non-intercepting technique to determine beam position but do not give any information about beam size. Beam size checks are required to make sure the

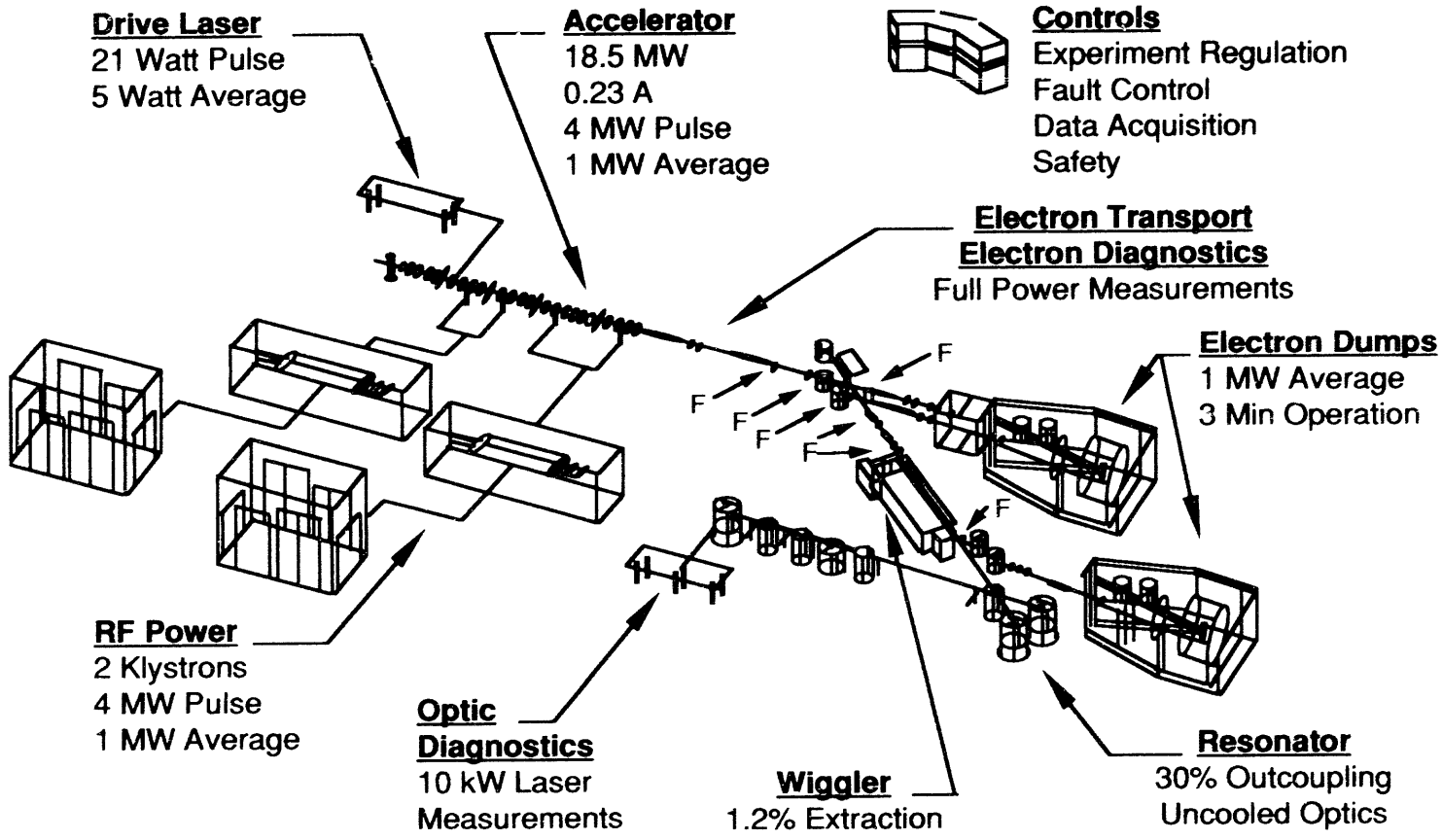

Figure 1. Schematic of the APLE / HPO. Flying wire locations are indicated by "F".

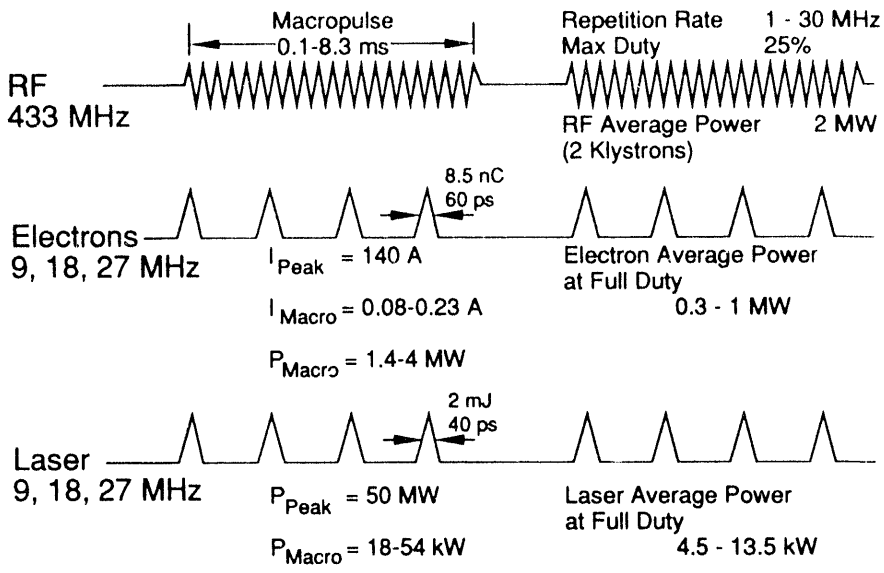

Figure 2. Pulse structure of the APLE / HPO RF, linac and laser.

beam remains stable and is not perturbed by RF loading and therefore remains matched to the wiggler as the pulse charge and duty factor are increased. Beam size measurements are also important for determining the energy spread by measuring the beam size in the bends and for determining the emittance by measuring the beam size at two or three consecutive positions in a focused region of the beam. Figure 3[2] is a plot of the nominal APLE/HPO beam size in the X and Y directions as a function of position through the machine. Note that the minimum beam size is about 0.1 cm.

To determine the beam size for high-duty operation at HPO, we have decided to use a scanning or "flying" wire that scans the beam in a time less than a single macropulse when the Linac is in high-duty operation. The selected positions for the flying wires are indicated by the letter F in Figure 1.

Previously, wire scanners have had a wide range of applications for measuring beam size at various accelerators and for various types of particles. Harp-like structures of tungsten wires have been slowly translated through the electron and positron beams at Stanford Linear Collider (SLC)[3] and Orsay[4] to determine beam size and position. Fine Be and C wire rapid-wire scanners, which translate the wires at up to 6 m/s, have been used to measure the beam size and emittance of protons and antiprotons at CERN.[5,6]

Table I. Summary of APLE/HPO Linac and Oscillator Parameters

E-beam	
Energy	18.5 MeV
Average power	1.04 MW
Peak current	140 A
Micropulse charge	8.5 nC
Normalized emittance	80π mm-mrad
Energy spread	0.3%
Micropulse rep rate	27 MHz
Wiggler	
Length	220 cm
Period	2.35 cm
Peak field	3.22 kG
Energy taper	4.6% nominal
Clear aperture	1 .15 cm
Bore ellipticity	2:1
Prebuncher	
Drift length	46.6 cm
Prebuncher length	21 cm
Period	2.70 cm
Peak field	1.67 kG
Resonator	
Length	16.6 m near concentric
Outcoupling	25%
Liltrow grating	10 lines/mm, 3 deg blaze angle

CERN has also made rapid wire scanner measurements of lepton beams using carbon wires where wire heating was a concern.[7] Fermilab also uses carbon flying wires rotated through ferrofluidic seals to monitor proton beams.[8]

Because of requirements described later, we must pass a carbon wire through the HPO beam at greater than 20 m/s. We based our design on the ground test accelerator (GTA) wire scanner,[9] which also must be scanned at a high rate of speed to measure the beam parameters of an intense proton beam. The GTA scanner features a carbon wire on an insulator wheel driven by a stepper motor and special controller through a ferrofluidic seal.

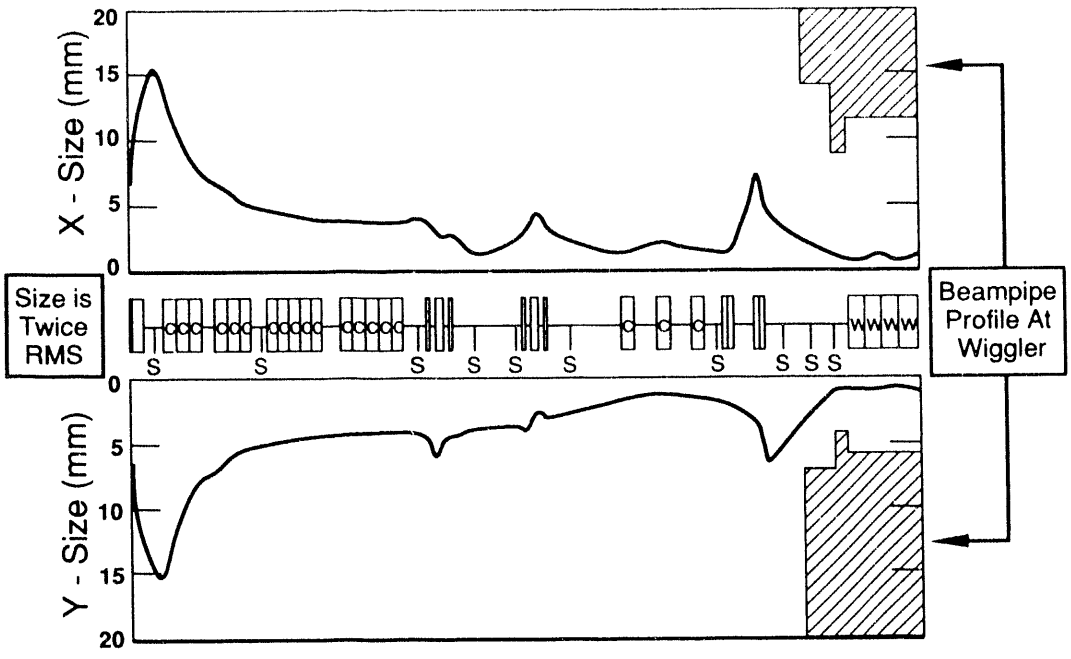

Figure 3. A plot of the nominal APLE / HPO beam size in the X and Y directions as a function of position through the machine.

This report describes the design and testing of the HPO flying wire prototype. The report begins as an expanded version of a previous paper[10] and we finish with the most recent information on the status of the actual flying wires being designed and built for HPO.

II. DETECTION SCHEMES

A. Bremsstrahlung

The Bremsstrahlung technique uses a radiation detector to detect the radiation generated as the wire intercepts the beam. The signal is assumed to be linearly related to the beam current intercepted by the wire. The technique was originally rejected because of the inconveniently narrow angular distribution of the Bremsstrahlung and the additional expense of the radiation detector.

The root mean square angular distribution for Bremsstrahlung is given by $\theta_{rms} = 1/\gamma$ radians or 27 mrad for 18.5 MeV electrons. The detector would have to be at least a meter downstream from the wire to intercept the radiation and would therefore be vulnerable to radiation from other sources such as background from beam loss. The detected signal would also possibly be sensitive to beam steering because of the narrow cone of the Bremsstrahlung.

We have since learned of SLC measurements where beam-wire interaction radiation was detected with a photomultiplier tube (PMT) next to the wire at a right angle to the beam. The PMT was shielded with collimators defining the line of sight. The signal was found to be linearly dependent on the beam-wire interaction. We are considering including a thinned region in the flying wire case so a PMT can be used at several stations should high-field emission, described below, prove to be a problem for the multistation emittance measurements where the beam may be focused to submillimeter size.

B. Secondary Emission

When an electron strikes a material, secondary electrons are emitted from the surface. The energy distribution of these electrons is in the 10 eV or less range[11, 12] and largely independent of primary electron energy. The efficiency for the process generally peaks at less than 2 secondary electrons per primary and for primary electron energies of less than 1 kV.[13] The efficiency gradually decreases with electron energy to a few percent in the 1 MeV and greater energy range. Measurements of yield of secondaries from carbon give a value of 1% for energies between 1 MeV and 1.6 MeV.[12] Assuming a 1% production rate, the secondary electron current is calculated to be on the order of 70 μA for a 35 μm wire centered in a 1 mm diameter, 0.2 A beam.

There are two methods for detecting secondary emission. Either the replacement current to the wire itself is measured or, because the secondary electrons have ~10 eV of energy, the secondary electrons can be collected with an anode type arrangement. Both techniques were tried during the beam tests described below.

III. DESIGN CONSIDERATIONS

A. Thermal Damage

The main concern is that the wire will be heated until it is damaged. The beam is capable of destroying beam tubes and shutoff valves in a few 10 s of microseconds. A wire must be durable enough and must be swept through the beam quickly enough to prevent damage.

The wire heating can be calculated knowing the number of incident particles, N, and the stopping power, dE/dx. The energy deposited, ΔE, in a volume V of material of density ρ and thickness V/A, where A is the area of interaction, is related to N and dE/dx as

$$N\frac{dE}{dx} = \frac{\Delta E}{\rho V}A \ . \qquad (1)$$

The change in temperature of this volume due to the deposited energy ΔE is given by

$$\Delta T = \frac{\Delta E}{CM} = \frac{\Delta E}{C\rho V} \qquad (2)$$

where M is the mass and C is the specific heat of the material. Substituting for ΔE in Equation 2 from Equation 1 gives

$$\Delta T = N\frac{dE}{dx}\frac{1}{CA} \ . \qquad (3)$$

Equation 3 shows that the figure of merit for wire heating is the ratio of dE/dx to C. Table II lists the values of dE/dx at 18.5 MeV,[14] C[13,15] and the ratio for several materials. Based on Table II, carbon and beryllium clearly have the advantage. Carbon has a higher melting point than beryllium. Carbon also has a high tensile strength and low mass making it suitable for surviving the mechanical stress from accelerations and decelerations. Therefore, carbon was selected for the flying wire. Although Table II lists a melting point of 3773 K for carbon, practical experience

Table II. Listing of Potential Wire Materials and Properties at 18.5 MeV and 1000 K

Material	Melt Pnt. (K)	Tens. Str. (psi)	C (cal/g K)	dE/dx (MeV cm^2/g)	dE/dx C
C	>3773	250,000[a]	0.45	2.12	4.70
Ti	2093	112,000	0.14	2.47	17.64
Al	933	30,000	0.28	2.28	8.14
Cu	1356	30,000	0.13	2.62	20.15
W	3653	500,000	0.35	3.55	10.14
Ni	1726	120,000	0.14	2.61	18.64
Be	1551	18,000	0.43	2.00	4.65

[a]Typical value. Values depend on the specifics of the fiber.

has shown that rapid-scanner wire failure will occur at much lower temperatures than 3773 K. For repeated scans, the practical safe limit seems to be about 2000 K.

The average number of electrons passing a given point per unit area of e-beam during a macropulse is I_M/ae where I_M is the average beam current during the macropulse, e is the electron charge and a is a representative area of the beam. The time for the wire to scan through the beam is ϕ/v where v is the speed of the wire and ϕ is some representative diameter of the beam. The number, N, of electrons that strike an area A of the wire in a single pass is given by

$$N = \frac{I_M}{e}\frac{\phi}{v}\frac{A}{a}. \tag{4}$$

If we assume a can be related to ϕ via $a = \pi\phi^2/4$ and substitute Equation 4 into Equation 3 we get

$$\Delta T = \frac{4}{\pi}\frac{I_M}{e}\frac{dE}{dx}\frac{1}{Cv\phi}$$

or

$$\Delta T = 3.04\times10^5\frac{dE}{dx}\frac{I_M}{Cv\phi} \tag{5}$$

where dE/dx is in MeV cm^2/g, I_M is in amps, C is in cal/g K, v is in cm/s and ϕ is in cm.

We can use Equation 5 to estimate the worst-case, single-pass wire heating for ϕ = 0.1 cm and I_M = 0.23 amps using the values for C and dE/dx from Table II. With v = 2000 cm/s, ΔT=1647 K, therefore elevating the wire temperature to 1940 K, which is below the practical wire failure temperature of 2000 K.

The rate for repeating scans is determined by the cooling time. The wire is in a vacuum and can only cool by radiation or conduction through the ends. The power radiated by a blackbody is given by

$$P = \frac{dE}{dt} = A_S\sigma T^4 \tag{6}$$

where we have used the same notation as previously with A_S defined as the surface area of the blackbody and σ is the Stefan-Boltzmann constant. The change in wire temperature is related to the change in temperature by Equation 2 with ΔT and ΔE replaced by dT and dE. Integrating Equation 6 and using the modified Equation 2 to replace dE gives

$$\frac{C\rho V}{A_S \sigma T^4} dT = dt. \tag{7}$$

We note that for a cylinder where the ends are ignored, $V/A_S = D/4$, where D is the wire diameter. After substitution and integration, the result is

$$\Delta t = \frac{C\rho D}{12\sigma} \frac{1}{T_1^3} - \frac{1}{T_2^3}$$

$$\Delta t = 3.68 \times 10^8 \frac{1}{T_1^3} - \frac{1}{T_2^3}, \tag{8}$$

where we used D = 35 μm and ρ = 3.5 g/cm^3. If T_2 = 2000 K and T_1 = 293 K, then from Equation 8, Δt = 15 s.

The conductive cooling time can be estimated from the solution to the linear heat transport equation,[16]

$$T_1 = \frac{\varepsilon}{\rho C (4\pi\chi\Delta t)^{1/2}} exp(-x^2 / 4\chi\Delta t), \tag{9}$$

where χ is the thermal diffusivity coefficient, x is the distance along the wire and ε is the energy per unit cross sectional area of the wire deposited by the beam at $t = 0$ and $x = 0$. Note that T_1 implies the temperature after cool down and Δt is the time required to reach T_1. If $x = 0$ is the center of the beam-wire interaction, then Equation 9 reduces to

$$T_1 = \frac{\varepsilon}{(4\pi\rho C\kappa\Delta t)^{1/2}} \tag{10}$$

where we used the relationship $\chi = \kappa/\rho C$. κ is the coefficient of thermal conductivity, which ranges from 0.06 to 15.0 W/cm/K for carbon depending on the form, crystal orientation and temperature.[13] We assumed a typical value of 1.5 W/cm/K.

Now $\varepsilon = \Delta E / a_w$ where a_w is the cross sectional area of the wire. From Equation 2, $\Delta E = C\rho V \Delta T = C\rho l a_w \Delta T$ where l, the length of the interaction region of the wire, is equal to ϕ, the beam diameter. Therefore we approximately have

$$\varepsilon = C\rho l \Delta T \quad . \tag{11}$$

Substituting Equation 11 into Equation 10 and solving for Δt we get

$$\Delta t = \frac{C\rho l^2}{4\pi\kappa} \frac{(\Delta T)^2}{T_1^2}$$

$$\Delta t = 3.42 \times 10^{-3} \frac{(\Delta T)^2}{T_1^2} \tag{12}$$

where we took $\rho = 3.5$ g/cm^3. Note that Equation 12 is a crude approximation because of the assumptions about the boundary conditions. The beam energy is deposited over a finite length of wire, and the wire is not infinitely long. If we take $T_1 \sim 300$ K and $\Delta T = 2000$ K, then Equation 12 gives $\Delta t = 0.15$ s.

In both the case of conductive and radiative cooling, the time required to cool the wire before another scan can be made is ≥ 0.1 s. Therefore it was not possible in the design to use a continuously scanned or rotating wire. For this reason, it was decided to design a wire that would accelerate from a parked position, scan the beam and decelerate into another parked position for cool down.

B. Thermionic Emission

A second consideration related to wire heating is the nonlinear increase in either replacement current or collected charge due to thermionic emission from the wire as it passes through the beam. Carbon melts at about 3800 K depending on the form. When materials approach 2000 K they can thermionically emit electrons. The passage of the beam drives the electrons away so that space charge does not limit the thermionic current. We can estimate when thermionic emission would be a problem using[11]

$$J = A_0 T^2 \exp(-w / kT) \tag{13}$$

where J is the emission current in A/cm^2, w is the work function and k is Boltzmann's constant. A_0 has the theoretical value of 120 A/cm^{2}K^2 but in practice can be as low as half this value because of surface contamination. The work function for carbon is 5 eV.[13] Assuming that the current is emitted from the surface of the wire at the region of beam interaction, the thermionic current is given by

$$I = \pi D \phi A_0 T^2 \exp(-w / kT)$$

$$I = 0.132 T^2 \exp(-5.80 \times 10^4 / T). \tag{14}$$

We again assumed a 0.1 cm diameter beam and 35 μm diameter wire. Figure 4 is a plot of Equation 14. It can be seen that thermionic current becomes a problem above 2400 K. Therefore, the temperature limitation due to the thermionic current is comparable to the practical temperature limit for wire damage.

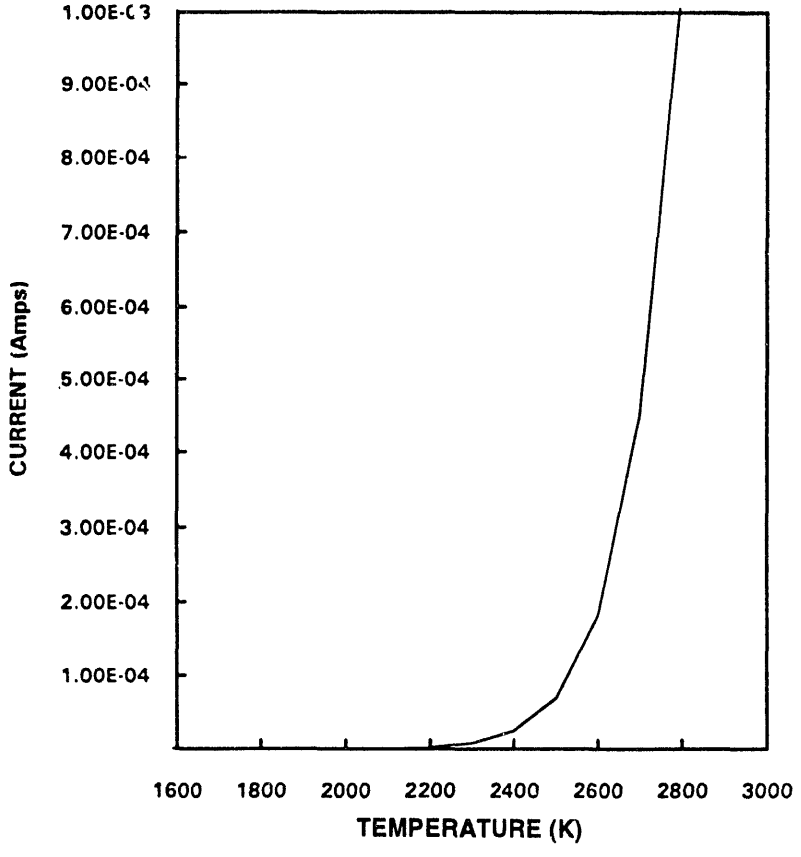

Figure 4. Graph of the calculated thermionic current from a 35 μm diameter carbon wire intersecting a 0.1 cm diameter beam versus wire temperature.

C. High-Field Emission

Another potential problem that we considered was the field induced emission of electrons from the wire. During the tests on APEX, described below, we intentionally focused a 50 μs macropulse, 3 nC/micropulse beam on a wire to determine the failure level. We focused the beam to less than a 200 μm diameter spot. Before wire failure, which required many macropulses, we observed a sudden increase in signal, at least an order of magnitude more than expected. As a high charge density pulse interacts with the wire, high local fields are generated. The high fields can eject electrons from the wire in addition to those ejected via secondary emission. This effect can be worse if the wire is also hot. The signal therefore increases non-linearly. For a cold surface, the high-field emission current per unit area, J, is related to the electric field, E, as

$$J = A_1 E^2 \exp(-b / E) \tag{15}$$

where A_1 is a material dependent constant and b is related to the material work function.[11] For large E, J goes as the square of the electric field. SLC has observed spontaneous emission and states that field emission is observed abruptly at 10^8 to 10^9 V/cm.[3] Fields of the order of 10^6 V/cm are adequate to initiate high-field emission.[17]

The field levels near a wire can be crudely estimated by assuming that the micropulse charge is contained in a sphere with a diameter equal to the average beam diameter ϕ. The field at the surface of a uniformly charged sphere of radius $\phi/2$ is given by

$$E_\phi = \frac{Q}{\pi \varepsilon_0 \phi^2}$$

$$E_\phi = 3.60 \times 10^3 \frac{Q}{\phi^2} \quad . \tag{16}$$

Here, the constant assumes Q, the micropulse charge, is in nanocoulombs and ϕ, the beam radius, is in centimeters; E will then be in V/cm. We note that because the beam is highly relativistic and the length of a beam pulse is ~10 ps (0.3 cm) in the laboratory frame, this approximation is crude.

Table III lists the calculated fields using the approximation in Equation 16 for various conditions. The SLAC beam conditions were taken from reference 3.

Table III. Calculated Maximum Micropulse Fields for Several Beams and Conditions

SLC obs. thresholds:	ϕ = 0.010 cm, Q = 1.5 nC then $E_\phi = 5.4 \times 10^7$ V/cm
	ϕ = 0.001 cm, Q = 0.3 nC then $E_\phi = 6.8 \times 10^7$ V/cm
APEX obs. thresholds:	ϕ = 0.020 cm, Q = 3.0 nC then $E_\phi = 2.7 \times 10^7$ V/cm
HPO max. expected flds:	ϕ = 0.100 cm, Q = 8.5 nC then $E_\phi = 3.1 \times 10^6$ V/cm

The APEX charge and beam diameter values in Table III were estimated from observations during the wire damage studies. It can be seen that the minimum HPO beam diameter and maximum micropulse charge generate maximum fields, which are an order of magnitude below those where spontaneous emission occurred at APEX and SLC. There may be a problem, however, during multiwire emittance measurements where the beam may be focused on a wire. See conclusions below.

IV. PROTOTYPE MECHANICAL DESIGN

The design and construction of the prototype used for tests on APEX was greatly aided by the existence of a flying wire scanner designed for the LANL ground test accelerator (GTA).[9] The GTA prototype had been built but only preliminary laboratory test data existed. The GTA requirements for wheel velocity were also less demanding.

The primary challenge of the mechanical design for the APLE flying wire was to accelerate the motor and wheel from rest to the required velocity and back to rest in less than one revolution. The acceleration must be smooth and reproducible, with minimal timing jitter when the wire passed through the beam. A Compumotor model KS-230 servomotor with indexer position control was chosen for this system. The motor was selected to provide sufficient torque to accelerate the motor and wheel to a velocity of 25 rps in less than half a revolution.

The ideal velocity profile should have a trapezoid shape, i.e., constant acceleration from rest up to the desired operating speed, followed by a period of constant velocity as the wires pass through the beam, and finally constant deceleration back to rest. However the inertia of the motor and wheel combined with the rapid change in velocity makes it difficult to achieve the ideal velocity profile. Figure 5 shows a plot of an ideal velocity profile

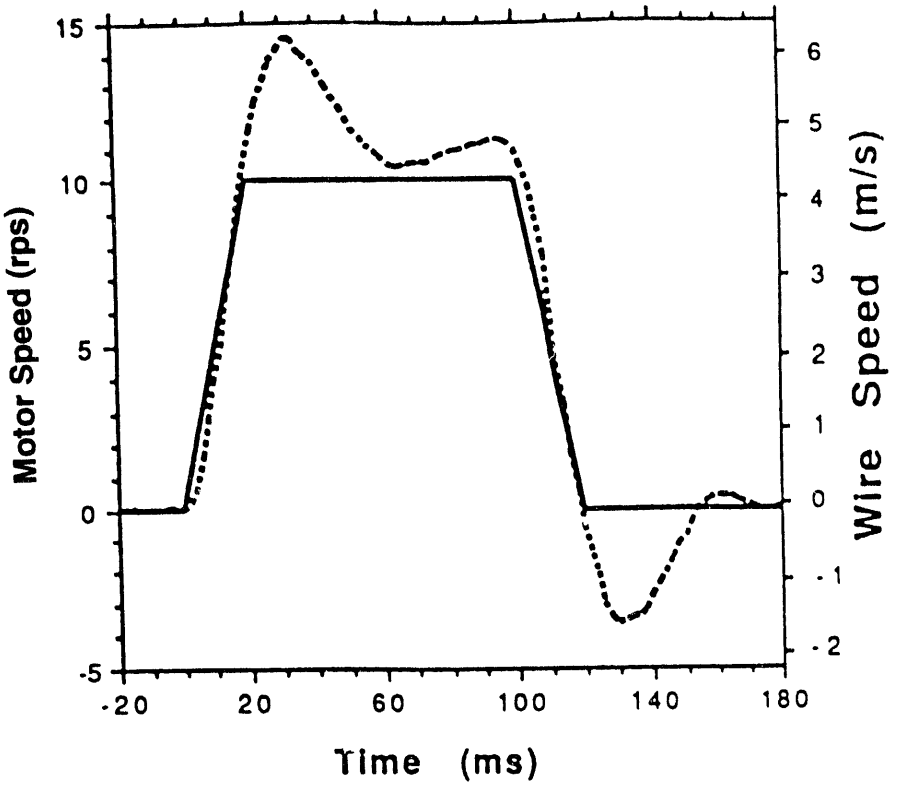

Figure 5. A plot of an ideal (solid) velocity profile specified by the indexer and an actual (dashed) profile measured by a tachometer mounted on the back of the motor.

specified by the indexer and an actual profile measured by a tachometer mounted on the back of the motor. There is considerable overshoot in the measured velocity due to the inability of the servomotor's closed loop control system to react fast enough to keep the motor on the specified velocity profile. However the transversal time of the wire through the beam is less than 1 ms. Therefore the velocity can be considered constant during the measurement. The motor speed is recorded along with the signal in order to determine the wire's velocity at the time of the measurement.

For the best performance the wheel must be both stiff and light-weight. Of the several materials (aluminum, G-10 fiberglass epoxy, and VESPEL [a polyimide]) that were tried, 1.6 mm thick G-10 was found to be the best. Because the one-spoke wheel tends to distort a small amount during acceleration and deceleration, the wires will break if they are rigidly attached to the wheel. Instead one end of each wire is attached to the wheel with a small spring, which helps maintain a constant wire tension. Using the spring attachment, the wires are able to survive over 10,000 cycles at a peak wheel speed of 25 rps. The electrical contacts to the wires were routed

through a hole in the shaft of the ferrofluidic feedthrough between the wheel in vacuum and the motor in air, and potted to maintain the vacuum seal. A short length of wire was left on the motor end of the ferrofluidic feedthrough to take up the slack as the motor rotated back and forth.

Two small rings were mounted on either side of the wire-beam intersection point to act as the charge collectors. The collector rings were connected in series to a vacuum feed through to an external connector.

V. PROTOTYPE ELECTRONIC DESIGN

The servomotor is controlled by a prototype VME indexer, designed and built at LANL.[18] This indexer was designed to replace commercially available indexers that tend to have timing jitter of up to a few milliseconds due to the cycle time of their onboard microprocessors, which must be interrupted to begin the control sequence. The LANL indexer has no onboard microprocessor. Instead the indexer has only memory that is loaded ahead of time with a bit pattern corresponding to the motor step sequence. Upon receipt of a trigger, the bit pattern is immediately read out at a constant rate determined by a clock frequency and used to drive the stepping motor. Using this indexer, the jitter between the trigger and the time the wheel rotates half a revolution, passing one of the wires through the beam center at a wheel speed of 25 rps, was measured to be 20 μs with respect to the external trigger.

A set of transimpedance amplifiers was designed and fabricated to convert the small secondary electron current to a voltage signal with a gain of 20,000 volts per ampere. The transimpedance amplifiers could also isolate the input and apply either a positive or negative bias of up to 300 V.

VI. BEAM TESTS

The system was tested using the electron beam provided by the APLE APEX FEL electron linac at LANL.[19-21] A schematic of APEX is shown in Figure 6. APEX is a photoinjector linac, which may be run at an energy of 20 to 40 MeV and a typical average beam current of 10 to 50 mA over a 5 to 20 μs long macropulse. The micropulses are typically 10-20 ps in length separated by 46 ns. The micropulse charge may be varied from 1 to 10 nC producing average currents of 0.02 to 0.20 amp during the macropulse. Figure 6 indicates the position of the flying wire at APEX during trial measurements. Figure 7 is a more detailed layout, which shows the arrangement of the OTR imager and the beam position monitor (BPM) relative to the flying wire. The OTR screen and video camera system were mounted 28 cm upstream of the flying wire. It would have been desirable to

APEX ELECTRON BEAM DIAGNOSTICS

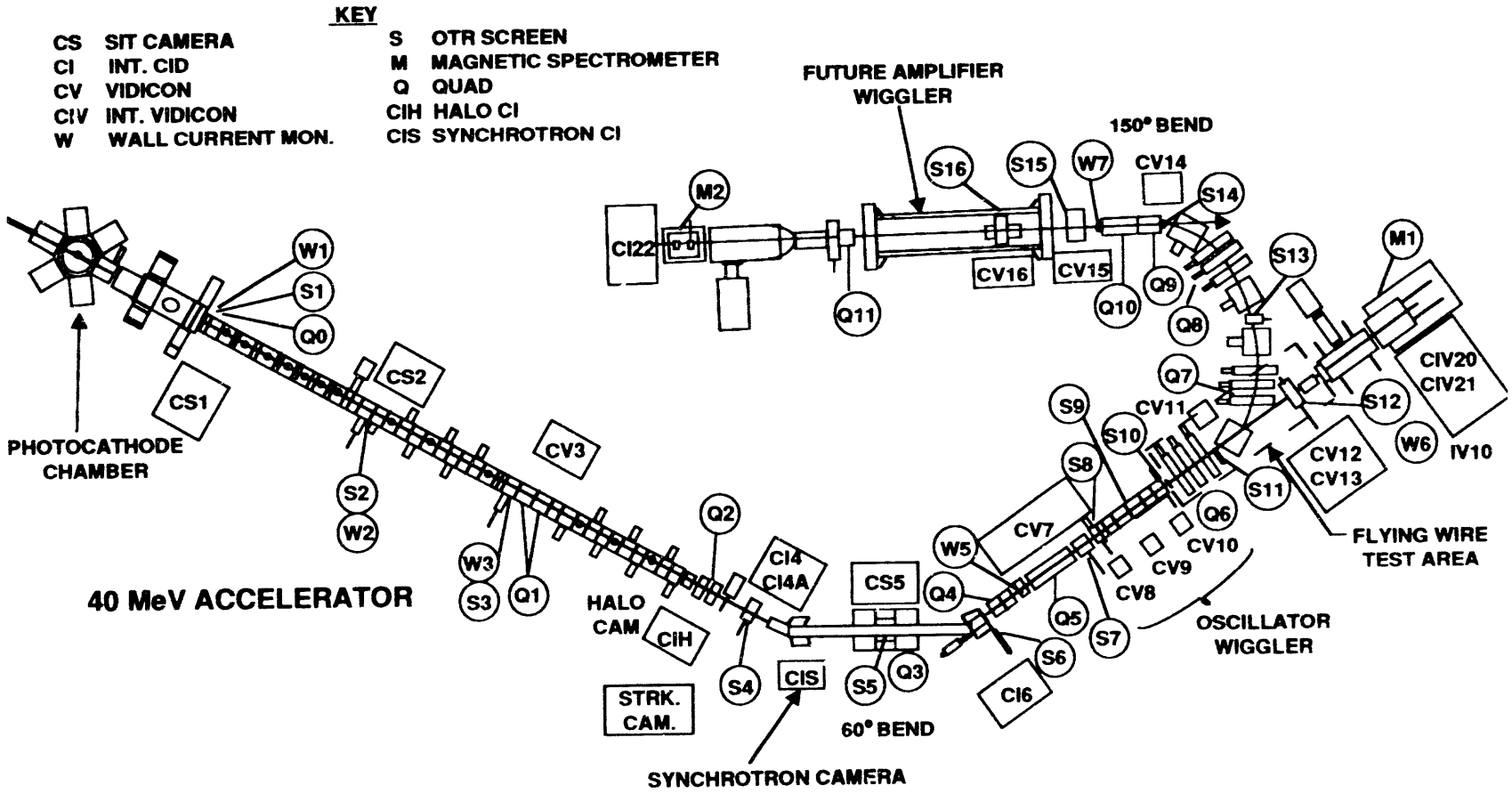

Figure 6. A schematic layout of APEX showing the location of the flying wire.

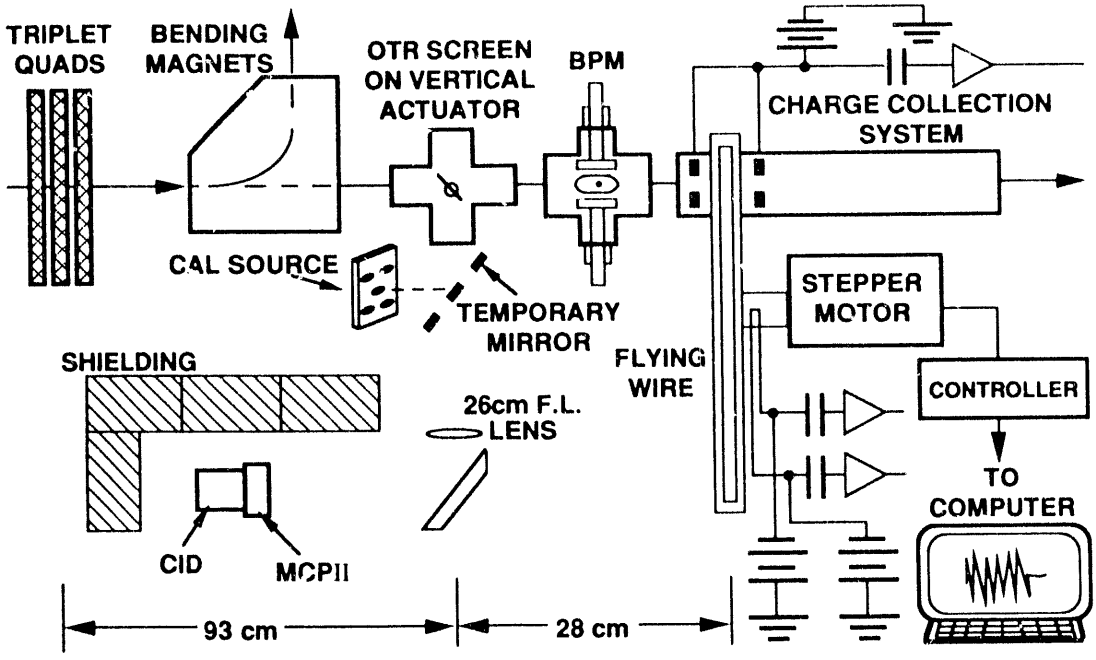

Figure 7. Detailed layout of the diagnostic arrangement used for the flying wire trial experiments on APEX.

mount the flying wire in front of the OTR screen. However, geometrical constraints in the region of the first section of the 120 degree bend precluded this happening.

The beam at the flying wire station was typically 1 to 4 mm in width. The short macropulse length of the APEX electron beam ruled out the possibility of operating the system in the flying-wire mode. However, the short macropulse and low duty factor of the APEX beam allowed the wires to be placed directly in the path of the beam for extended periods of time and many macropulses without being overheated. Therefore, we stepped the position of the wire through the beam and measured the signal on a macropulse to macropulse time scale to obtain the beam profile.

A. Wire Signals and Data Reduction

The first goal of the APEX beam tests was to determine the best means of detecting the beam and wire interaction so that the profile could be obtained. Figure 8 shows the signal from the wires and charge collector obtained during the beam tests. The micropulse charge was 0.4 nC with a 22 MHz frequency. The macropulse length was 5 μs. APEX was operated at its design electron energy of 40 MeV. Instabilities during 20 MeV operation made it difficult to take image and wire scan data, so we elected not to duplicate the HPO beam energy. Wire signal levels at 20 MeV were similar to the 40 MeV data. Wire number 1 was centered in the beam. The wire signals

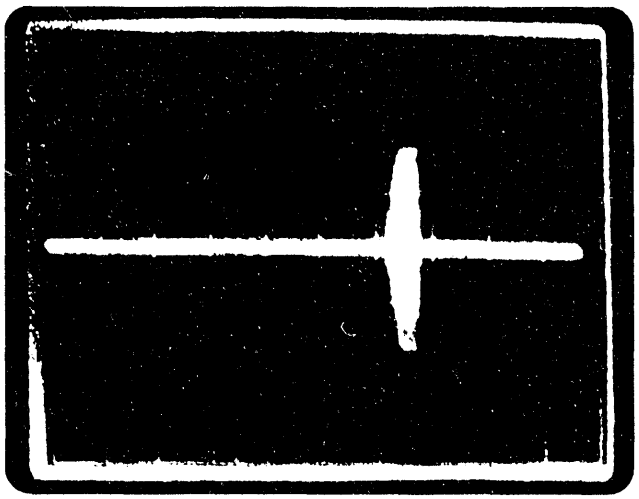

a) Collector Signal 50mV/ 10μs/

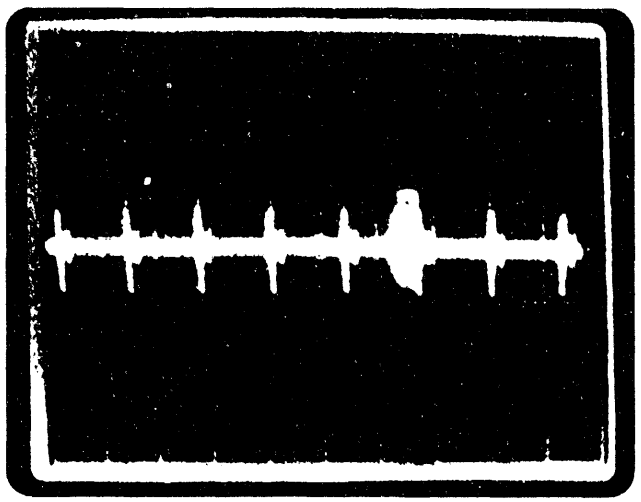

b) Wire #1 Signal 20mV/ 10μs/

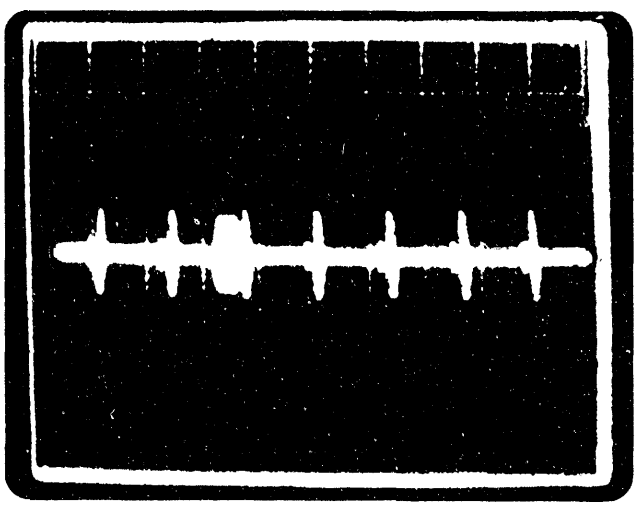

c) Wire #2 Signal 20mV/ 10μs/

Figure 8. Flying wire and charge collector signals during trial tests for a 40 MeV, 0.4 nC per micropulse, 22 MHz, 5 μs long macropulse beam. Wire #1 was centered In the beam.

are positive and the collector signal is negative. The bipolar signal during the time the beam is on is due to capacitive pickup from the detectors. The signal from wire number 1 is 5 mV with 15 mV of background pickup and 5 mV of noise not including the periodic spikes. We confirmed the spikes were due to pickup from the stepper motor driver, which is present whether the wire is being moved or not. The collector gave 35 mV of signal with 85 mV of background and less than 1 mV of noise. Therefore the signal to noise ratios are 0.33 and 0.41, respectively.

The collector background level in Figure 8 is unusually high. The S:N ratio was typically 10:1. The source of the collector background is not completely understood but is believed to be due to secondary electrons produced by the interaction of the beam with the walls of the beam pipe possibly from halo. The collector pickup could be varied by changing the tune on the beam, and large background could be generated by intentionally scraping the beam with the wall upstream. We hope to lower this type of background on the HPO flying wire by recessing the charge collectors in the wall of the beam tube. The collector signal was the same when either wire 1 or 2 was centered in the beam. The signals from wires 1 and 2 appeared equivalent when either was centered in the beam. In Figure 8, the signal from the collector is bigger than the wire signals because of different amplification.

The poor signal to noise ratio of the wires is attributed to the ~1 kΩ resistance of the carbon wires, which makes them good antennas for picking up noise. Applying a negative bias potential of a few hundred volts did not have any measurable effect on the wires' signal to noise ratio. The signal to noise ratio of the charge collector was found to be almost an order of magnitude better than the wires'. However the charge collectors had a background level of about 10%. The background subtracted signal from the collectors was comparable to the signal measured from the wires, indicating that the collection efficiency was near 100%. The signal measured from the wires and collectors was consistent with a secondary emission rate of about 1% per incident electron which is consistent with reference 12.

B. OTR Images and Data Reduction

The second goal of the APEX beam tests was to see how well the secondary electron signal from the wires could determine the beam profile by comparing the OTR images with the profile measured using the wire.

The imaging system used to obtain images for comparison with wire data is shown in Figure 7. An OTR screen was used to form an image of the beam. The image was relayed to an 18 mm diameter microchannel plate

image intensifier (MCPII) via turning mirrors and a 260 mm focal length, f/5 lens with a factor of 2X demagnification. The MCPII was fiber-optically coupled to a CID camera. A temporary mirror indicated by the dashed line in Figure 7 was used to image a resolution target. The layout of the resolution target is shown in Figure 9. The target was at a distance from the camera equivalent to the camera to OTR-screen distance. The resolution target also provided the image scale. The images were digitized on a VME 8-bit digitizer gen-locked to the video, which was read out with a work station over Ethernet.

The images were reduced on a work station using commercially available software. The "raw" images were first displayed as shown in Figure 10, which is an image of the resolution target of Figure 9. The OTR images are oriented so that they appear as if an observer were looking into the electron beam. The images are rotated 45 degrees to correspond to the orientation of the wires as shown in Figure 11. A box average of rows and

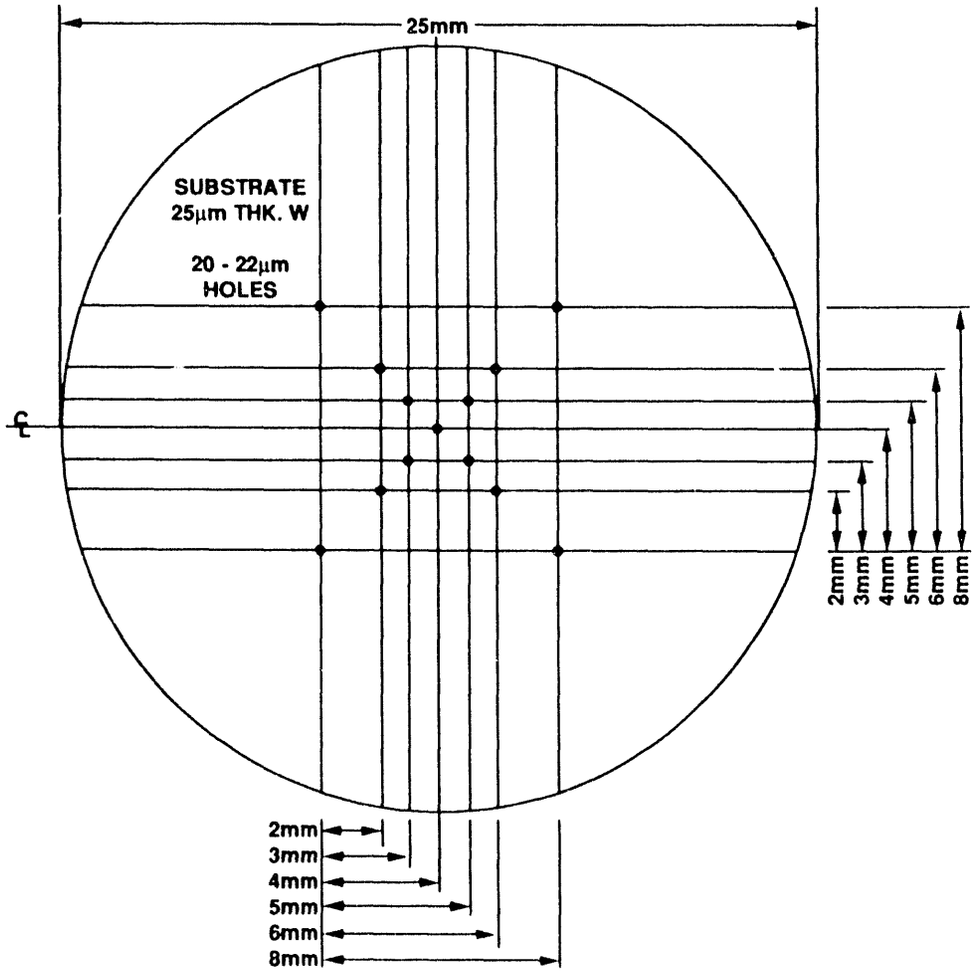

Figure 9. Target used for spatial calibration and determination of the system resolution.

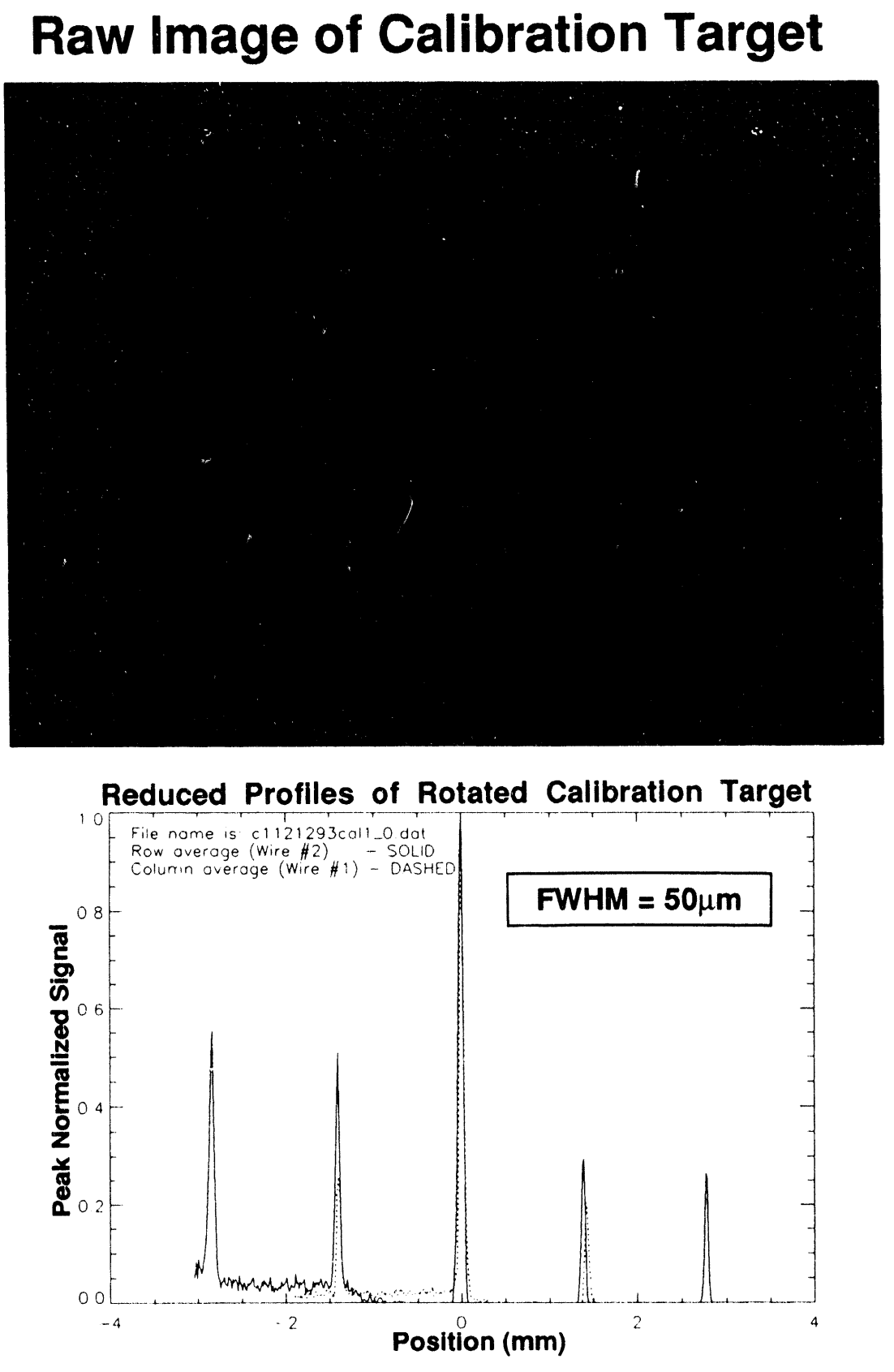

Figure 10. Image of the target shown in Figure 9 and the resulting plots after image reduction.

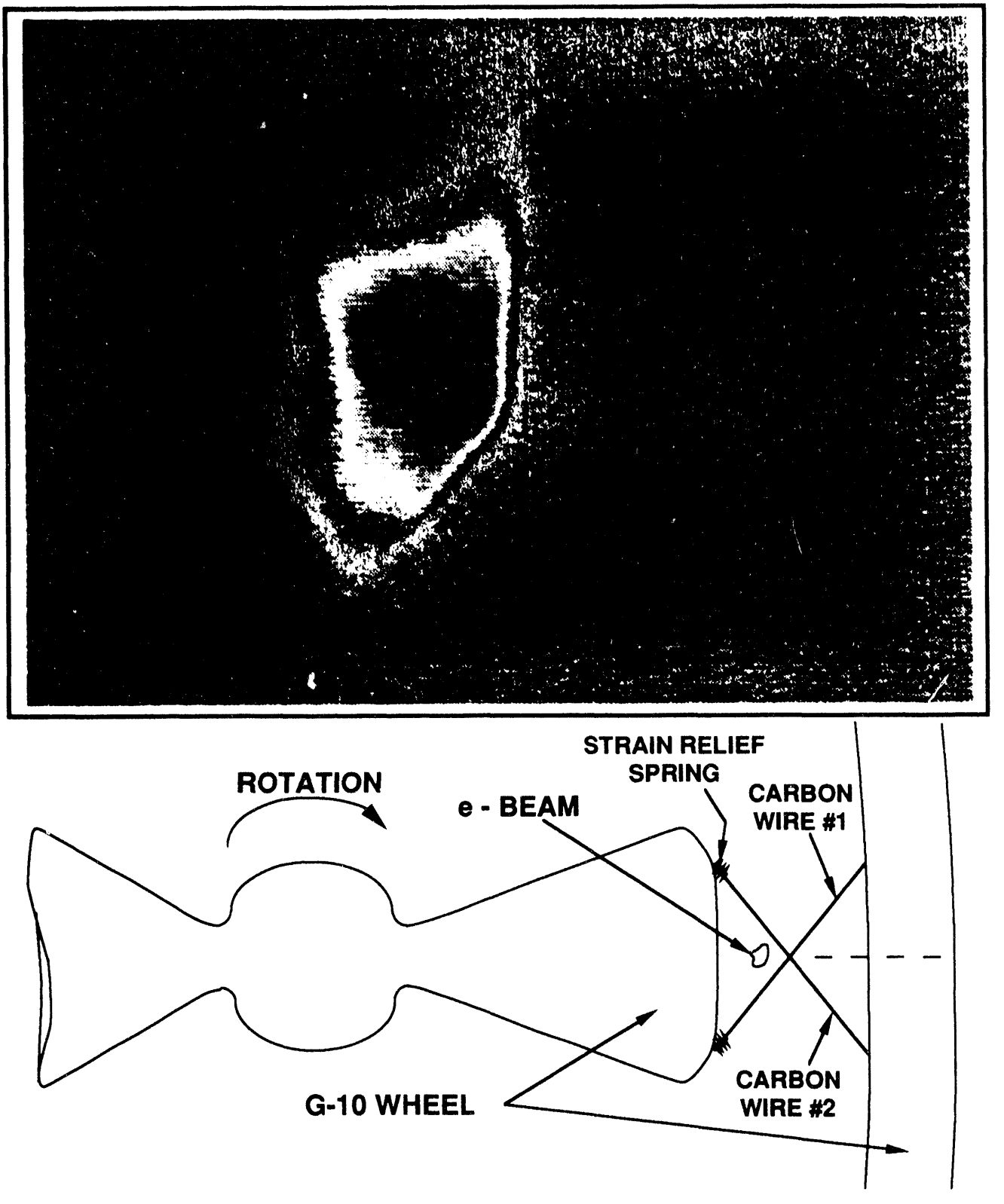

Figure 11. Raw OTR-screen image of electron beam compared with a schematic showing orientation of the flying wires relative to the beam. Beam image orientation is equivalent to looking into the beam.

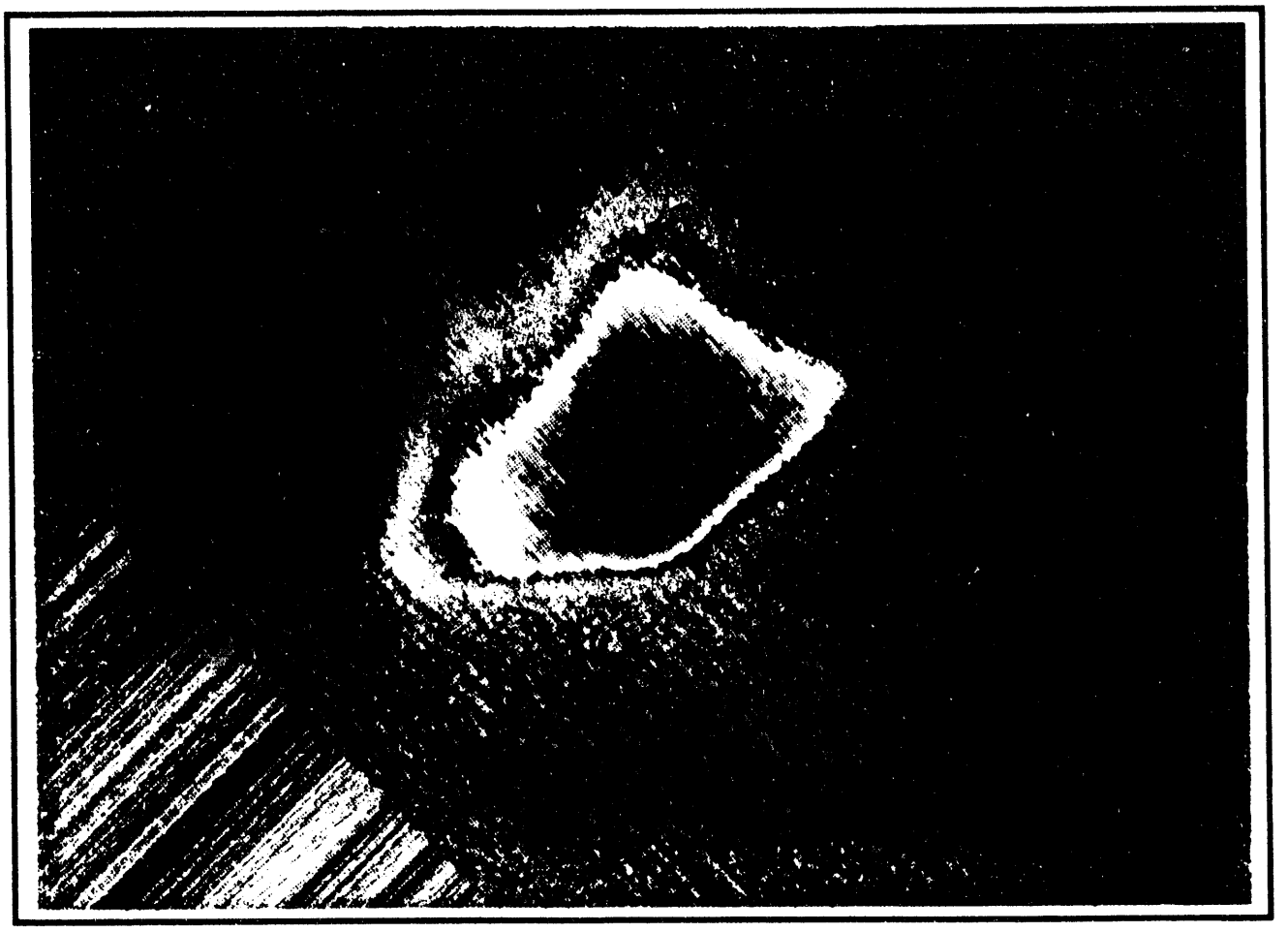

Figure 12. Results of applying data reduction procedures to beam image.

columns from a box placed around the rotated image is used to generate profiles for comparison with wire #2 and #1, respectively. It is necessary to plot the X-transpose of the profiles for comparison. The profiles are also peak normalized to 1 and scaled in the X-direction to millimeters. A constant scaling factor was used to normalize the width of the profile measured with the flying wire with the width of the OTR profile to account for the expansion of the beam over the drift between the OTR screen and the flying wire. The resulting profiles for the resolution and scaling target of Figure 9 are shown in Figure 10.

Figures 11 and 12 show the results of applying the reduction technique to actual data. Figure 11 shows the orientation of the image relative to the wires. Figure 12 shows the rotated image and the final plots of the image profiles corresponding to wire #1 (the dashed curve) and wire #2 (the solid curve).

C. Results

A 40 MeV, 1 nC per micropulse, 10 μs long macropulse was used while comparing the image profile to the scanned profile. Figure 13 shows a comparison between the OTR image data of Figures 11 and 12 and flying wire data taken at approximately the same time with wire #2. The flying-wire profile measurements were made using the charge collection rings with

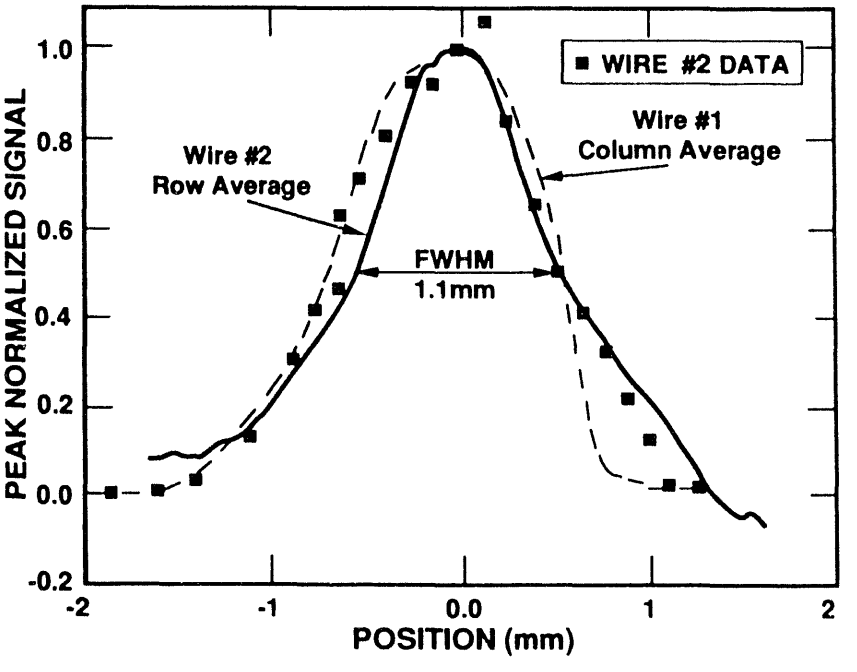

Figure 13. Comparison of beam profile measured with wire 2 and the charge collector and the equivalent profile obtained from the OTR image.

the background subtracted. Because the beam position tends to jitter and the wire location is downstream from the OTR screen, we expected some error in comparison between the image generated profile and the scanned profile. We tuned APEX for maximum stability and stepped the wire through the beam as quickly as possible requiring about 20 minutes. The beam FWHMs of about 1 millimeter show good agreement. The wire profile not only reproduces the beam width, it also follows the bump on the right side of the profile. As a more severe test, we focused the beam to a 0.65-mm spot. The OTR profiles and data taken with wire #1 are shown in Figure 14. Note the increased noise on the wire profile that results because the scan of the more tightly focused beam is more sensitive to jitter. The profiles again show good agreement.

VII. HPO DESIGN STATUS

From the experience on APEX and further refinement of HPO requirements, we have recently arrived at a set of specifications for the APLE/HPO flying wires. The current listing of specifications is given in Table IV. The specifications are nearly finalized and will not change much in the future.

Figure 15 shows the current design schematic. The major modification to the GTA design is the mounting of the stepper motor at a right angle to the

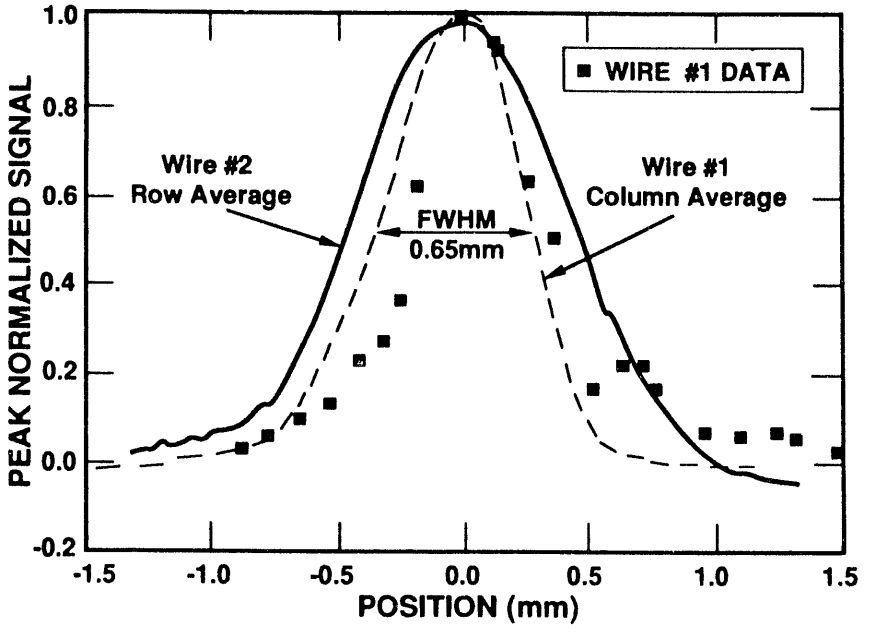

Figure 14. Comparison of a narrow beam profile measured with wire 1 and the charge collector and the equivalent profile obtained from the OTR image.

Table IV. Specifications for the APLE/HPO Flying Wire

REQUIRED ITEMS

Item	Vendor	Part No. Required	Spares	Total
Mechanical assembly	LANL	8	1	9
Wheel	LANL	8	4	12
Motor	Compumotor, ML2340	8	1	9
Driver	Compumotor, BLX75	8	1	9
Tachometer	Robyns & Meyers, M100	8	1	9
Transimpedance amp	LANL	8	3	11
Indexer	LANL	1	1	2
Multiplexer	ITI, Model 92114	1	0	1
VME crate	Tracwell, System 21	1	0	1
Transient digitizer	Omnibyte, Comet	1	1	2
GPIB interface module	Natl. Inst. EH1014	1	0	1
Delay generator	Mizan 8310	1	0	1

MEASUREMENT SPECIFICATIONS

Measurement	Specification
Profile resolution (FWHM)	75 μm
Lowest resolved beam current	0.02 mA
Bandwidth of detection system	200 Hz - 350 KHz
Expected practical noise	2 mV into 50 Ω
Trigger to beam intercept timing jitter	100 μs
Maximum repetition rate	1 Hz
Beam signal detection method	Secondary electron collection
Collector bias voltage	0 to +300 V
Secondary electron rate	1% of intercepted beam
Peak secondary electron current	100 μA for a 1 mm beam
Transimpedance amp gain	Remotely variable from 1,000 to 20,000 V/A
Relative wire position determination	Wheel velocity
Wheel velocity determination	Analog tachometer
Relative position uncertainty	50 μm

Table IV (continued)

ELECTRONICS AND CABLE SPECIFICATIONS

Item	Specification
Driver to motor cable	10' or 25' cable supplied with motor
Motor to drive cable	10' or 25' cable supplied with motor
Indexer to driver cable signals	16 strand twisted pair cable suitable for TTL level
Tachometer output cable	BNC
Transimpedance amp output cable	BNC (From Amp to control room)
Transimpedance amp input cable	SMA (From Amp to flying wire)
Transimpedance amp gain control	4 wire from amp to control room
Control interface	VME
Digitizing rate	1 MS/s
Trigger timing jitter	<50 μs
Space required in control room	1 VME crate, 1 multiplexer, and 1 delay generator
Space required in tunnel	Room for driver and signal amp within 25' of each flying wire

MECHANICAL SPECIFICATIONS

Item	Specification
Wheel material	G-10 Fiberglass/Epoxy Laminate
Wire material	35 μm carbon filament
Assembly outgas rate	5.0E-6 l/s
Assembly length (flange to flange)	≤ 25 cm
Typical wire speed	≥ 10 m/s
Typical wheel speed	24 rps
Beam pipe connectors	2" conflat

EXPECTED BEAM PARAMETERS

Parameter	Specification
Peak average beam current	0.23 A
Minimum beam width	1 mm
Beam energy	18 MeV

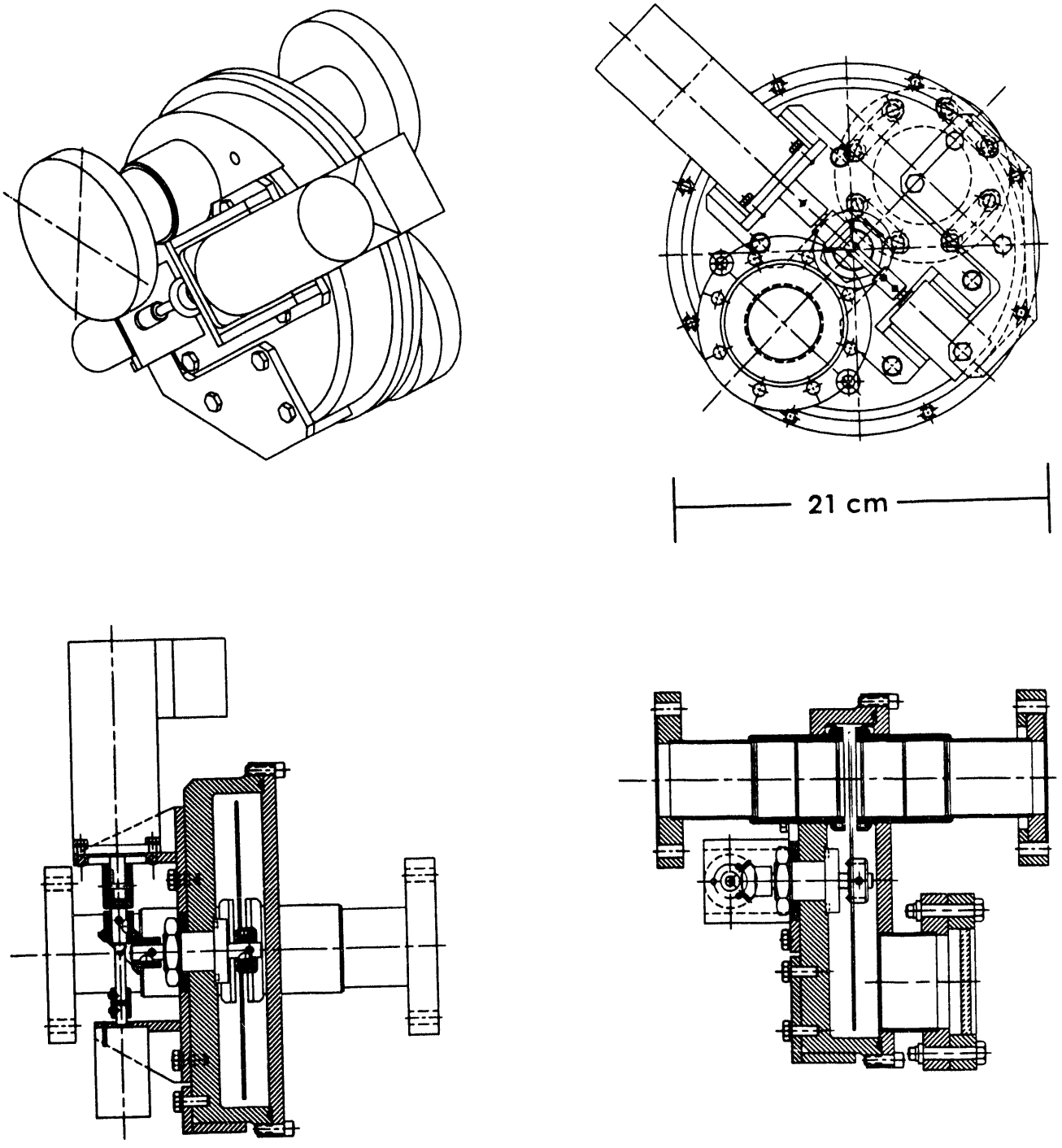

Figure 15. Schematic of the current design of the APLE / HPO flying wire.

beam line. This modification will require less space in the beam line. Work is proceeding on this design and prototype construction will soon begin.

Figure 16 is a block diagram of the control and data acquisition.[22] The interface with the Boeing control system[23] has been defined. LANL will provide the software to control the wire, acquire the data, analyze the data, and produce a simple result (i.e., beam profile plot and FWHM) in near real time. The hardware is well defined and selection is underway. Software and user interface are still in the definition stage. Boeing will supply the work station that will communicate with the flying wire system over VMI (VME extension for instrumentation) bus.

VIII. CONCLUSIONS AND RECOMMENDATIONS

The tests of the GTA prototype flying wire in the lab and on APEX show that it will work as a beam profile monitor on APLE/HPO. We currently observe a high level of noise, which limits the sensitivity of the secondary electron collection method. At the current noise levels we can still meet specifications. We expect that additional improvements on the mechanical and electrical design of the HPO/APLE flying wire will result in significant improvement of the wire performance.

Because of the possible requirement to make multiwire emittance measurements where the beam may be focused to a smaller diameter than the nominal 1 mm, we will modify the design to accommodate a radiation detector. The addition of the radiation detector will permit profile measurements in case spontaneous field induced emission proves to be a problem for the station near beam focus. In addition, space should be allocated near the emittance flying wire stations for inclusion of the radiation detector and lead collimation. We recommend that, initially, we only use the secondary collection method and add the radiation detectors if necessary. It should be noted from Equation 5 that overcoming the spontaneous field emission limit permits only a small decrease in spot size before the wire reaches the thermionic-emission and melting limits. Therefore, the immediate addition of the radiation detectors would probably not be cost-effective. We should wait to see how severe the need is. If we operate the beam at 9 MHz, Equation 5 and Table II indicate the wire would fail for spot sizes smaller than 160 μm.

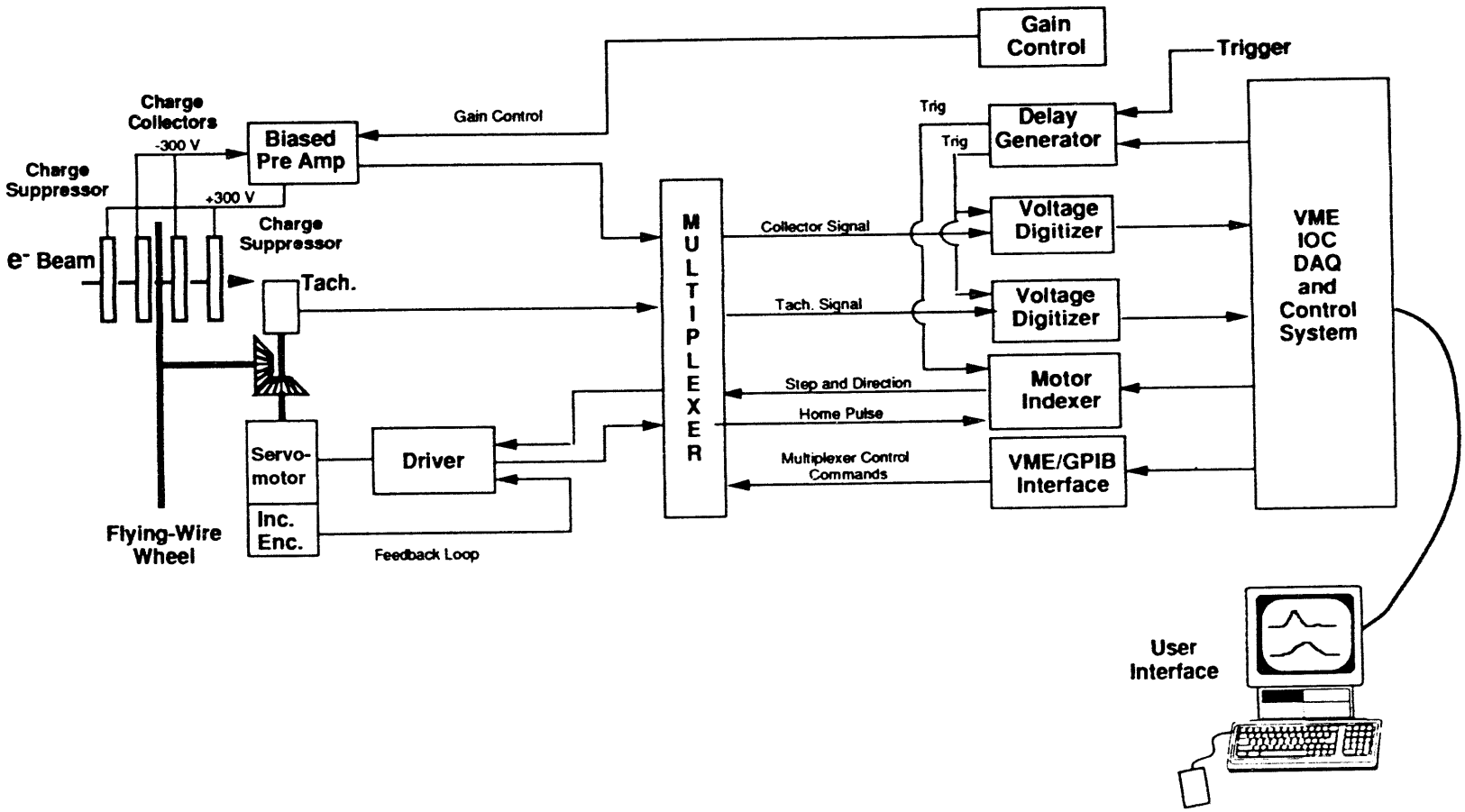

Figure 16. Block diagram of the flying wire data acquisition and control system for the APLE / HPO FEL.

ACKNOWLEDGMENTS

The authors are most grateful to Scott Apgar and Clinton Webb for their assistance in making the measurements on APEX. We also thank Tom Zaugg, Paul Ortega, Jim Early, and Jerry Barton for operating the linac and Patrick O'Shea, Don Feldman, and Alex Lumpkin for advice on making the measurements. Special thanks to Kathy Derouin and Gerald Martinez for their work in preparing this report.

REFERENCES

1. Adamski, J., "System Description," proceedings of System Final Design Review of Free Electron Laser Program Average Power Laser Experiment, Vol. 1, Oct. 20, Seattle, WA (1992).

2. Parazzoli, C., Rodenburg, R., and Quimby, D., "APLE High Power Oscillator Performance Predictions," proceedings of System Final Design Review of Free Electron Laser Program Average Power Laser Experiment, Vol. 1, Oct. 20, Seattle, WA (1992).

3. Ross, M. C., "Wire Scanner Systems for Beam Size and Emittance Measurements at SLC," in Particles and Fields Series 44, Acc. Instr. 2nd annual workshop, McGrory, E., (Ed.), AIP Conf. Proceed. 229, Batavia, Ill., p. 88 (1990).

4. Chehab, R., Bonnard, J., Humbert, G., Leblond, B., and Saury, J. L., "A Multiwire Secondary Emission Profile Monitor for Small Emittance Beams," IEEE Trans. Nuc. Sci., Vol. NS-32, 5, p. 1953, Oct. (1985).

5. Bosser, J., Camas, J., Evans, L., Ferioli, G., Hopkins, R., Mann, J., and Olsen, O., "Transverse Emittance Measurement with a Rapid Wire Scanner at the CERN SPS," Nuc. Inst. Meth. A235, p. 475 (1985).

6. Barisy, A., Bellone, R., Blanchard, R., Camas, J., Evans, L., Ferioli, G., Hopkins, R., Sievers, P., and Zanasco, J. P., "A Transverse Beam Profile Monitor for p-p^- Studies in the CERN SPS," IEEE Trans. Nuc. Sci., V NS-28, 3, p. 2180 June (1981).

7. Burns, A., Camas, J., Amico, E. D., Ferioli, G., King, Q., Kissler, K. H., Mann, J., and Schmidt, R., "Wire Scanner News from the CERN-SPS," Proc. 1989 IEEE Part. Acc. Conf., p 1580 (1989).

8. Gannon, J., Crawford, C., Finley, D., Flora, R., Groves, T., and MacPherson, M., "Flying Wires at Fermilab," Proc. 1989 IEEE Part. Acc. Conf., p. 4 (1989).

9. Fortgang, C. M., private communication and notes.

10. Barlow, D. B., Fortgang, C. M., Gilpatrick, J. D., Meyer, R. E., Rendon, A. M., Warren, D. S., and Wilke, M. D., "Prototype Flying-Wire Beam-Profile Monitor," submitted to 1993 Particle Accelerator Conf., Wash. DC, LA-UR-93-1827, May 17-20 (1993).

11. Fink, D. G. and McKenzie, A. A., (Ed.), Electronics Engineers' Handbook, McGraw-Hill Book Company, New York, 1st. Edit. (1975).

12. Schultz, A. A. and Pomerantz, M. A., "Secondary Electron Emission Produced by Relativistic Primary Electrons," Phys. Rev., V. 130, 6, p. 2135, June (1963).

13. Weast, R. C., Astle, M. J., and Beyer, W. H., CRC Handbook of Chemistry and Physics, CRC Press Inc., Boca Raton, FL, 64th Edit. (1983).

14. Gray, D. E., (Ed.), American Institute of Physics Handbook, McGraw-Hill Book Company, New York, 3rd. Edit. (1972).

15. Forsythe, W. E., Smithsonian Physical Tables, The Lord Baltimore Press, Baltimore, MD, 9th. Edit. (1956).

16. Zel'dovich, Ya. B. and Raizer, Yu. P., Physics of Shockwaves and High-Temperature Hydrodynamic Phenomena Volume II, Hayes, W. D., and Probstein, R. F., (Ed.), Academic Press Inc., New York, NY (1967).

17. Howatson, A. M., An Introduction to Gas Discharges, Pergamon Press, Oxford, U. K., 2nd Edit. (1976).

18. Fortgang, C. M., "Conceptual Design and Requirement Document for the Flying Wire Indexer," Los Alamos National Laboratory, LA-CP-90-446 (1990).

19. O'Shea, P. G., Bender, S. C., Byrd, D. A., Carlsten, B. E., Early, J. W., Feldman, D. W., Feldman, R. B., Johnson, W. J. D., Lumpkin, A. H., Schmitt, M. J., Springer, R. W., Stein, W. E., and Zaugg, T. J., "Initial Results from the Los Alamos Photoinjector-Driven Free-Electron Laser," Nuc. Inst. Meth., A318, p. 52 (1992).

20. O'Shea, P. G., Bender, S. C., Carlsten, B. E., Early, J. W., Feldman, D. W., Feldman, R. B., McKenna, K. F., Schmitt, M. J., Springer, Stein, W. E., Wilke, M. D., and Zaugg, T. J., "Performance of the 40-MeV

Photoinjector-Driven Linear Accelerator," Proc. Advanced Accel. Concepts Workshop by the AIP, Brookhaven Nat. Lab., Upton, NY, June 14 (1992).

21. Feldman, D. W., Bender, S. C., Byrd, D. A., Carlsten, B. E., Early, J. W., Feldman, R. B., Goldstein, J. C., Martineau, R. L., O'Shea, P. G., Pitcher, E. J., Schmitt, M. J., Springer, Stein, W. E., Wilke, M. D., and Zaugg, T. J., "Operation of the APEX Photoinjector Accelerator at 40 MeV," LA-UR-92-2645, Proc. 16th Inter. Linac Conf. Ottawa, Ontario, August 23-28 (1992).

22. Greegor, R. and Wilke, M., "E-Beam Diagnostics," proceedings of System Final Design Review of Free Electron Laser Program Average Power Laser Experiment, Vol. 2, Oct. 21, Seattle, WA (1992).

23. Milliman, L., Regan, A., and Lancaster, C., "Controls," proceedings of System Final Design Review of Free Electron Laser Program Average Power Laser Experiment, Vol. 2, Oct. 21, Seattle, WA (1992).

*U.S. GOVERNMENT PRINTING OFFICE 1994-0-573-024/7014

DATE

FILMED

8/9/94

END